LUNAR ELECTRICAL CONDUCTIVITY, PERMEABILITY, AND TEMPERATURE

FROM APOLLO MAGNETOMETER EXPERIMENTS

P. Dyal, C. W. Parkin, and W. D. Daily

Ames Research Center
Moffett Field, Calif. 94035

University of Santa Clara
Santa Clara, Calif. 95053

and

Brigham Young University
Provo, Utah 84602

Lunar Electrical Conductivity, Permeability, and Temperature
from Apollo Magnetometer Experiments

by

P. Dyal

NASA-Ames Research Center, Moffett Field, CA 94035

C. W. Parkin

Univ. of Santa Clara, Santa Clara, CA 95053

W. D. Daily

Brigham Young Univ., Provo, UT 84602

Lunar Electrical Conductivity, Permeability, and Temperature
from Apollo Magnetometer Experiments

P. Dyal*, C. W. Parkin**, and W. D. Daily***

Abstract---Magnetometers have been deployed at four Apollo sites on the moon to measure remanent and induced lunar magnetic fields. Measurements from this network of instruments have been used to calculate the electrical conductivity, temperature, magnetic permeability, and iron abundance of the lunar interior. Global lunar fields due to eddy currents, induced in the lunar interior by magnetic transients, have been analyzed to calculate an electrical conductivity profile for the moon. From nightside magnetometer data in the solar wind it has been found that deeper than 170 km into the moon the conductivity rises from 3×10^{-4} mhos/m to 10^{-2} mhos/m at 1000 km depth. Recent analysis of data obtained in the geomagnetic tail, in regions free of complicating plasma effects, yields results which are consistent with nightside values. Conductivity profiles have been used to calculate the lunar temperature for an assumed lunar material of olivine. In the outer layer ($\sim$170 km thick) the temperature rises to 1100°C, after which it gradually increases with depth to 1500°C at a depth of $\sim$1000 km. Simultaneous measurements by magnetometers on the lunar surface and in orbit around the moon are used to construct a whole-moon hysteresis curve, from which the global lunar magnetic permeability is determined to be $\mu = 1.012 \pm 0.006$. The corresponding global induced dipole moment is 2×10^{18} gauss-cm^3 for typical inducing fields of 10^{-4} gauss in the lunar environment. Lunar free iron abundance corresponding to the global permeability is determined to be 2.5 ± 2.0 wt%. Total iron abundance (sum of iron in the ferromagnetic and paramagnetic states) is calculated for two assumed compositional models of the lunar interior. For a free iron/orthopyroxene lunar

*NASA-Ames Research Center, Moffett Field, CA 94035
**Univ. of Santa Clara, Santa Clara, CA 95053
***Brigham Young Univ., Provo, Utah 84601

1

composition the total iron content is calculated to be 12.8 ± 1.0 wt%; for a free iron/ olivine composition, total iron content is 5.5 ± 1.2 wt %. Other lunar models with an iron core and with a shallow iron-rich layer are also discussed in light of the measured global lunar permeability. The measured lunar remanent fields range from 3 gammas (γ) minimum at the Apollo 15 site to 327 γ maximum at Apollo 16. Simultaneous magnetic field and solar plasma pressure measurements show that the remanent fields at the Apollo 12 and 16 sites interact with, and are compressed by, the solar wind. Remanent fields at Apollo 12 and 16 are increased 16 γ and 32 γ, respectively, by a solar plasma bulk pressure increase of 1.5×10^{-7} dynes/cm^2. Velocities and thicknesses of the earth's magnetopause and bow shock have been estimated from simultaneous magneto-meter measurements. Average speeds are determined to be about 50 km/sec for the magnetopause and 70 km/sec for the bow shock, although there are large variations in the measurement for any particular boundary crossing. Corresponding measured boundary thicknesses average to about 2300 km for the magnetopause and 1400 km for the bow shock.

INTRODUCTION

In this paper we discuss the experimental results and analyses from magnetometer experiments deployed by astronauts on the surface of the moon in the Apollo program. Measurements from this network of instruments at the Apollo 12, 14, 15, and 16 landing sites (shown in Figure 1) have been used to calculate the magnetic permeability, Fig. 1 electrical conductivity, and temperature of the lunar interior. The fossil remanent magnetic fields have been measured at the four landing sites and the magnetic field interaction with the solar wind plasma has been measured at three of the sites.

Simultaneous magnetic field measurements by the Explorer 35 lunar orbiting satellite and the Apollo surface experiments have been analyzed to determine the time dependence of eddy-current induction in the moon by solar field transients. This analysis has yielded a continuous electrical conductivity profile from which an internal temperature profile is calculated for assumed lunar material compositions. Similarly, magnetic field measurements obtained when the moon is immersed in the steady geomagnetic tail are used to construct a global hysteresis curve, from which the magnetic

permeability of the lunar interior is determined. The iron abundance of the moon is then calculated for different compositional models of the lunar interior.

The remanent magnetic field has been measured at the Apollo 12, 14, 15, and 16 landing sites. The two photographs in Figure 2, taken by the Apollo 16 astronauts, show the two magnetometers used to measure remanent and induced fields at the Apollo 16 Descartes site. The remanent magnetic field provides a record of the magnetic field environment that existed at the moon 3.7 to 4.2 billion years ago at the time the crustal material cooled below its Curie temperature. The remanent field is found to be compressed by the solar wind plasma, and the properties of the compression are used to study the scale size and topology of the field. Simultaneous measurements obtained with this network of magnetometers on the lunar surface are also used to determine the thickness and velocity of the earth's bow shock and magneto-sheath. The positions of these boundaries relative to the lunar orbit are shown in Figure 3.

ELECTRICAL CONDUCTIVITY AND TEMPERATURE OF THE LUNAR INTERIOR

Electrical conductivity and temperature of the moon have been calculated from global eddy current response to changes in the magnetic field external to the moon. When the moon is subjected to a change in the external field, an eddy current field is induced in the moon which opposes the change (see Figure 4). The induced field responds with a time dependence which is a function of the electrical conductivity distribution in the lunar interior. Simultaneous measurements of the transient driving field (by Explorer 35) and the lunar response field (by an Apollo surface magnetometer) allow calculation of the lunar conductivity. Since conductivity is related to temperature, a temperature profile can be calculated for an assumed compositional model of the lunar interior.

When the moon is in the solar wind, lunar eddy current fields form an induced lunar magnetosphere which is distorted in a complex manner due to flow of solar wind plasma past the moon. The eddy current field is compressed on the dayside of the moon and is swept downstream and confined to the "cavity" on the lunar nightside. Because of the complexity, early analysis included a theory for transient response of a sphere in a vacuum in order to model lunar response as measured on the lunar

nightside (Dyal et al., 1970a; Dyal and Parkin, 1971a; Sill, 1972); a harmonic theory of a sphere totally confined by the solar wind was used to model the response as measured on the lunar dayside (Sonett et al., 1971, 1972; Kuckes, 1971; Sill, 1972). Both the transient and the harmonic techniques have subsequently been further developed. Transient analysis has evolved to include effects of cavity confinement on nightside tangential data and to introduce analysis of magnetic step transients measured on the lunar dayside (Dyal and Parkin, 1973; Dyal et al., 1973). Harmonic analysis has been developed with the purposes of eventually developing a dynamic response theory for the case of asymmetric confinement (Schwartz and Schubert, 1973) and of extending the data analysis to lower frequencies and accounting for diamagnetic effects in the solar wind (Kuckes et al., 1974).

Recently time-dependent poloidal response of a sphere in a vacuum has been applied to data measured in the geomagnetic tail where plasma confinement effects are minized. The poloidal response analysis has been used to determine the electrical conductivity and temperature profiles of the lunar interior.

Electrical conductivity analysis: moon in solar wind plasma

1. Lunar nightside data analysis. The lunar electrical conductivity has been investigated by analysis of the lunar response to transients in the solar wind magnetic field. The response, measured by an Apollo magnetometer on the nightside of the moon, is theoretically approximated by the response of a conducting sphere in a vacuum. The theory was developed by extending the work of Smythe (1950) and Wait (1951) for a radially varying lunar conductivity profile (Dyal et al., 1972a). The measured response (illustrated in Figure 5a) is the average poloidal field response (for the radial surface field component) to a normalized fast-ramp decrease in the external field. Error bars are standard deviations of the measured responses. Chosen for the analysis is a ramp input function which falls from unity to zero in 15 seconds, a time characterizing convection of a solar wind discontinuity past the Moon. (For a 400 km/sec solar wind, this time is 10-20 sec, depending on the thickness of the discontinuity and the inclination of its normal to the solar wind velocity).

For a family of conductivity profiles, all of which monotonically increase with depth in the moon, the theoretical response to a fast ramp is calculated and compared to the

Fig. 5

measured response. A particular set of these conductivity profiles yield response functions which pass within all data error bars of Figure 5a. These profiles define the shaded region of Figure 8 and are all consistent with the nightside response data.

2. Lunar dayside data analysis. Theoretical solutions for an eddy current field totally confined to a sphere of homogeneous conductivity are derived from Maxwell's equations in Dyal et al. (1973). Figure 5b shows averages of normalized rising step transients measured on the lunar dayside in response to increasing step transients in the free-streaming solar wind (error bars are standard deviations). The overshoot maximum is amplified by a factor of 5 over the external input field step change, by solar wind dayside confinement of the surface tangential field components. The data are fit by a lunar conductivity model with a homogeneous core of radius $R_c = 0.9R_m$ and conductivity $\sigma \sim 10^{-3}$ mhos/m. This result is consistent with the nightside conductivity profile illustrated in Figure 8 to depths allowed by the duration of the response data which is shown in Figure 5b.

Electrical conductivity analysis: moon in the geomagnetic tail

The theoretical models outlined so far have all assumed spherical symmetry to describe lunar eddy current response to changes in the external field. However, the nightside and dayside analyses have used data taken when the moon is immersed in the solar wind plasma with asymmetric confinement of the inducing fields. The shortcomings of using spherically symmetric approximations to describe the induced lunar magnetosphere, which is actually asymmetrically confined, have been pointed out in the literature for both the nightside vacuum approximation (see e.g., Schubert et al., 1973a) and the dayside totally-confined approximation (see, e.g. Dyal and Parkin, 1973). Three-dimensional, dynamic asymmetric confinement presents a difficult theoretical problem which has not been solved at the time of this writing. Previous theoretical approximations of the asymmetric problem have included a two-dimensional approximation (Reisz et al., 1972); three-dimensional static theory for a point-dipole source, with substantiating laboratory data (Dyal and Parkin, 1973); a three-dimensional "quasi-static" approach (Schubert et al., 1973b); and a three-dimensional dynamic theory for one particular orientation of variations in the external field (Schwartz and Schubert, 1973). In order to circumvent this problem of asymmetry, recent analysis has considered lunar eddy current response during times when the moon is in the geomagnetic tail where plasma

5

interaction effects encountered in the solar wind (asymmetric confinement, remanent field compression, plasma diamagnetism, etc.) are minimal.

1. Poloidal response of a sphere in a vacuum: theory.

To describe the response of lunar sphere to an arbitrary input field in the geomagnetic tail, we define the magnetic vector potential $\underline{A}$ such that $\nabla \times \underline{A} = \underline{B}$ and $\nabla \cdot \underline{A} = 0$. We seek the response to an input $\Delta \underline{B}_E b(t)$, where $b(t) = 0$ for $t < 0$ and $b(t)$ approaches unity as $t \rightarrow \infty$. (Since the governing equations are linear, the response to a more general input is readily found by superposition.) The direction of $\Delta \underline{B}_E$ is taken to be the axis of a spherical coordinate system (r, θ, φ). If the conductivity is spherically symmetric, the transient magnetic field response has no φ component, and hence $A = A\hat{e}_\varphi$ and $\partial/\partial \varphi = 0$. Under these conditions (and neglecting displacement currents) the laws of Faraday, Ampere, and Ohm combine to yield a diffusion equation for the magnetic potential (in MKS units):

$$\nabla^2 \underline{A} (r, \theta; t) = \mu \sigma (r) \frac{\partial \underline{A}}{\partial t} (r, \theta; t) \tag{1}$$

We will show in a later section on magnetic permeability that we may take $\mu \tilde{=} \mu_o$ everywhere. Then, for $t > 0$, the magnetic field must be continuous at the surface, so that $\underline{A}$ and $\partial A/\partial r$ must always be continuous at $r = R_m$, the radius of the sphere. We also have the boundary condition $A(0, t) = 0$ and the initial condition $\underline{A}(r, \theta, \varphi) = 0$ inside the moon. Outside of the moon, where $\sigma = 0$,

$$A = \Delta B_E \left(\frac{r}{2}\right) b(t) \sin\theta + \frac{\Delta B_E}{r^2} f(t) \sin\theta . \tag{2}$$

The first term on the right is a uniform magnetic field modulated by $b(t)$; the second term is the (as yet unknown) external transient response, which must vanish as r and $t \rightarrow \infty$. Note that at $r = R_m$, where R_m is normalized to unity,

$$A = \Delta B_E \sin\theta \left(\frac{b(t)}{2} + f(t)\right) \tag{3}$$

and

$$\frac{\partial A}{\partial r} = \Delta B_E \sin\theta \left(\frac{b(t)}{2} + 2f(t)\right) . \tag{4}$$

Therefore, at $r = R_m = 1$,

$$\frac{\partial A}{\partial r} = -2A + \frac{3}{2}\left(\Delta B_E \sin\theta\, b(t)\right).$$

(5)

Since the magnetic field is continuous at $r = R_m$, this is a boundary condition for the interior problem. Letting $G(r, t) = A/\Delta B_E \sin\theta$ and $\bar{G}(r, s)$ be the Laplace transform of G, equation (1) becomes

$$\frac{1}{r}\left(\frac{\partial^2}{\partial r^2}(r\bar{G}) - \frac{2}{r}\bar{G}\right) = s\mu_0\sigma(r)\bar{G}$$

(6)

for the interior. The boundary conditions are

$$\frac{\partial \bar{G}}{\partial r} = -2\bar{G} + \frac{3}{2}\bar{b}(s)$$

(7)

at $r = R_m$ and

(8)

$$\bar{G} = 0$$

at $r = 0$.

For a given $\sigma(r)$ and $b(t)$, this system is numerically integrated to obtain $\bar{G}(r, s)$ in the range $0 \leq r \leq R_m$. The function $\bar{G}(r, s)$ is then numerically inverse Laplace transformed to find the characteristic transient response function $f(t)$ for the system. The resulting $f(t)$ is compared to the measurements and reiterated with a different function $\sigma(r)$ until the error between the calculated $f(t)$ and the measured $f(t)$ is minimized. The final $\sigma(r)$ is not unique; rather a family of $\sigma(r)$ is generated with the constraint that $f(t)$ match the experimental data.

2. Conductivity results: geomagnetic tail data analysis. Figure 6 shows an example of a magnetic transient measured in the geomagnetic tail. The data components are expressed in a coordinate system which has its origin on the lunar surface at the Apollo 12 magnetometer site. The x-component is directed radially outward from the lunar surface, while the y-and z-components are tangent to the surface, directed eastward and northward, respectively. The external (terrestrial) driving magnetic field is measured by Explorer 35, whereas the total response field is measured on the lunar surface by the Apollo 12 magnetometer.

Fig. 6

To analyze this and similar events, the Explorer 35 input field components are fitted numerically by functions which are sums of ramp inputs chosen to fit the external field data. For a given conductivity model of the moon, the theoretical time series response to an external field data set is numerically calculated using the theory outlined in the previous section. This calculated response is then compared with the measured Apollo 12 time series data. Conductivity profiles have been constrained to be monotonically increasing with depth into the moon.

Figure 7 shows an example of calculated response for the Explorer 35 x-axis (radial) input function of Figure 6, using the conductivity profile illustrated in Figure 7. Superimposed is the actual response, which is the Apollo 12 x-component of Figure 6. This conductivity profile yields the best fit of seventy profiles which have been run to date, although it is certainly not unique. The profile also yields theoretical responses which fit well for the measured tangential components of Figure 6 and the components of twenty other geomagnetic tail transients which have been processed to date. The analysis presented here is still preliminary; in the future many more transient events will be processed to determine a range of conductivity profiles consistent with a large data set.

In the previous sections various techniques which we have utilized to investigate lunar electrical conductivity were surveyed. Figure 8 shows a summary of conductivity profiles which have been calculated.

Lunar temperature profiles from conductivity analyses. Once the electrical conductivity profile of the moon has been determined, an internal temperature distribution can be inferred for an assumed lunar material composition (see Rikitake, 1966). For cases where electrical conductivity is independent of pressure to a first approximation, the conductivity of materials can be expressed in terms of temperature T as follows:

$$\sigma = \sum_i E_i \exp\left(-a_i/RT\right) \tag{9}$$

where a_i are the activation energies of impurity, intrinsic, and ionic modes, expressed in electron volts; E_i are material-dependent constants; and k is Boltzmann's constant. It should be emphasized that the electrical conductivity σ (a, E, T) is a strong function

of the material composition; therefore, uncertainties in knowledge of the exact composition of the sphere limits the accuracy of the internal-temperature calculation.

Laboratory results relating conductivity to temperature for various minerals, which are good geochemical candidates for the lunar interior, have been presented by many investigators (e.g., England et al., 1968; Schwerer et al., 1972; Olhoeft et al., 1973; Duba et al., 1972; Duba and Ringwood, 1973). The recent work by Duba et al. (1972) on the electrical conductivity of olivine has been used to convert the electrical conductivity profiles of Figure 8 to the temperature profiles shown in Figure 9.

MAGNETIC PERMEABILITY AND IRON ABUNDANCE IN THE MOON

Magnetic permeability and iron abundance of the moon are calculated by analysis of magnetization fields induced in the permeable material of the moon. When the moon is immersed in an external field it is magnetized; the induced magnetization is a function of the distribution of permeable material in the interior. Under the assumption that the permeable material in the moon is predominately free iron and iron-bearing minerals, the lunar iron abundance is calculated from the lunar permeability for assumed compositional models of the interior. Since the amount of iron present in the lunar interior should be consistent with the measured global magnetic permeability, the permeability in effect places a constraint on the physical and chemical composition of the moon's interior.

Global magnetic permeability

Deployment of Apollo magnetometers on the lunar surface has allowed simultaneous measurements of the external inducing field (by Explorer 35) and the total response field at the lunar surface (by an Apollo magnetometer). During times when eddy current induction fields and interaction fields are negligible, the total response field measured at the surface by an Apollo magnetometer can be expressed:

$$\underline{B} = \mu \underline{H} = \underline{H} + 4\pi \underline{M} \tag{10}$$

e $\underline{H}$ is the external magnetizing field and $\underline{M}$ is the magnetization field induced

e permeable lunar material (see Figure 10). The relative magnetic permea-

r is $\mu = 1 + 4\pi k$, where k is magnetic susceptibility in emu/cm^3. Since the

ar magnetization $\underline{M}$ is known to be below the Explorer 35 magnetometer reso-

n (Behannon, 1968), it is assumed in the dual magnetometer analysis that

orer 35 measures $\underline{H}$ alone.

For the two-layer lunar permeability model illustrated in Figure 10 (which

be referred to later when iron abundance calculations are considered), the total

at the outer surface of the sphere is expressed

$$\underline{B} = H_x(1 + 2G)\,\hat{x} + H_y(1-G)\,\hat{y} + H_z(1-G)\,\hat{z} \qquad (11)$$

'e

$$G = \frac{(2\eta+1)(\mu_1-1) - \lambda^3(\eta-1)(2\mu_1+1)}{(2\eta+1)(\mu_1+2) - 2\lambda^3(\eta-1)(\mu_1-1)} \qquad (12)$$

$\eta = \mu_1/\mu_2$; μ_1 and μ_2 are relative permeability of the shell and core, respectively.
permeability exterior to the sphere is $\mu_o = 1$, that of free space; $\lambda = R_c/R_m$;
nd R_m are radius of the core and the moon, respectively. Equation (11)
esses the total surface field in a coordinate system which has its origin on the
r surface at an Apollo magnetometer site: $\hat{x}$ is directed radially outward from
unar surface, and $\hat{y}$ and $\hat{z}$ are tangential to the surface, directed eastward and
iward, respectively.

A plot of any component of equation (11) will result in a B – H hysteresis curve.
ition (12) relates the slope of the hysteresis curve to the lunar permeability. The
age whole-moon permeability μ is calculated from the hysteresis-curve slope by
ng $\mu_1 = \mu_2 = \mu$ in equation (3):

$$G = \frac{\mu - 1}{\mu + 2} \qquad (13)$$

The hysteresis-curve method of permeability analysis was first employed by
and Parkin (1971a) to calculate the whole-moon permeability result 1.03 ± 0.13.
e then the error limits have been lowered by processing a larger number of
iltaneous data sets and using more rigid data selection criteria (e.g., Parkin
., 1973).

In the most recent dual-magnetometer results (Parkin et al., 1974a, b), a

hysteresis curve has been constructed using 2703 data sets (see Figure 11). Since the external magnetizing field is so small (~10 gammas), the familiar "S" shape of hysteresis curve degenerates to a straight line (Ellwood, 1934). The data have been fitted by a least squares technique which yields the slope best estimate of $1.008 \pm$ 0.004. Using this value with the radial (x) component of equation (11) and equation (13), the whole-moon permeability has been calculated to be $\mu = 1.012 \pm 0.006$ (2 σ error limits). Both extrema are greater than 1.0, implying that the moon, as a whole, acts as a paramagnetic or weakly ferromagnetic sphere. This result has been used to calculate the iron abundance of the moon as discussed in the next section.

Russell et al. (1974) have recently made permeability calculations using data from a single magnetometer, the Apollo 15 subsatellite magnetometer orbiting at an altitude about 100 km above the moon. The results to date indicate that the relative permeability of the entire spherical volume enclosed by the satellite orbit is below 1.0, implying that the layer between the moon and the satellite orbit is diamagnetic. Whether such a layer exists is uncertain at this time; further investigation is required using both magnetic and plasma data.

Lunar iron abundance

Iron abundance calculations have been presented by various authors, in theoretical treatments based on geochemical and geophysical properties calculated for bodies of planetary size (Urey, 1962; Reynolds and Summers, 1969; Urey and MacDonald, 1971) or on measured compositions of meteorites (Wänke et al., 1973). Recently the global lunar permeability measurement, determined from magnetic field measurements, has been modeled by a homogeneous paramagnetic rock matrix (olivine and orthopyroxene models are used), in which free metallic iron is uniformly distributed. Pyroxenes and olivines have been reported to be major mineral components of the lunar surface fines and rock samples (Nagata et al., 1971; Zussman, 1972; Weeks, 1972), with combined iron present at the paramagnetic Fe^{2+} ion. The ferromagnetic component of lunar samples is primarily metallic iron which is sometimes alloyed with small amounts of nickel and cobalt (Nagata et al., 1972; Pierce et al., 1971). This free iron is thought to be native to the moon (because of its low nickel content) rather than meteoritic in origin (Strangway et al., 1973a). Orthopyroxene and olivine models are consistent with

Fig. 11

11

)chemical studies (Urey et al., 1971; Wood et al., 1970; Ringwood and

sene, 1970; Green et al., 1971) and geophysical studies (Toksöz, 1974).

Since the susceptibility of free iron changes several orders of magnitude at

iron Curie temperature (T_c), a two-layer model has been used, with the

re-shell boundary R_c at the Curie isotherm (see Figure 10). For $R > R_c$,

T_c. Therefore, for $R > R_c$ any free iron is ferromagnetic while at greater

)ths where $T > T_c$, the free iron is paramagnetic. The Curie isotherm location

determined from the thermal profile used for a particular model. Three thermal

)dels have been used in the calculations. For model profile T_1 the Curie isotherm

spherically symmetric and located at $R_c/R_m = 0.9$. Shell and core temperatures

$= 600^\circ C$ and $1400^\circ C$, respectively. For the model profile T_2 the shell is $500^\circ C$,

d the core is $1300^\circ C$, while the Curie isotherm boundary is at $R_c/R_m = 0.85$.

mperatures are $300^\circ C$ and $700^\circ C$ for shell and core of model profile T_3, which has

$/R_m = 0.7$. In the outer shell there are both ferromagnetic and paramagnetic

ntributions to the total magnetic permeability $\mu_1 = 1 + 4\pi k_1$. The susceptibility of

shell is $k_1 = k_{1c} + k_{1a}$, where k_{1a} is "apparent" ferromagnetic susceptibility and

is paramagnetic susceptibility. The ferromagnetic component is metallic free

n, assumed to be composed of multidomain, noninteracting grains; the paramagnetic

nponent is Fe^{2+} combined in the orthopyroxene or olivine rock matrix. The measured

·romagnetic susceptibility of the shell material is an apparent value which differs from

intrinsic ferromagnetic susceptibility of the iron because of self-demagnetization of the

1 grains and the volume fraction of iron in the shell. For $R < R_c$ the lunar material is

amagnetic only, with susceptibility $k_2 = k_{2c} + k_{2a}$; k_{2c} is the contribution of paramagnetic

·mically combined iron and k_{2a} is the apparent susceptibility of free paramagnetic iron

)ve the Curie temperature.

From the magnetic properties of lunar compositional and thermal models, lunar

n abundances have been calculated for the moon which are consistent with measured

)bal permeability (Parkin et al., 1974a,b). The results are summarized in

gure 12. The minimum total iron abundance consistent with the hysteresis curve can   Fig. 12

lculated assuming the whole-moon permeability corresponds entirely to ferromagnetic

)n in the outer shell where the temperature is below the Curie point. For this case

e bulk iron abundance is 0.9 ± 0.5 wt. %. It is noted that the susceptibilities of both

ivine and orthopyroxene are about an order of magnitude too small to account for the

measured permeability without some ferromagnetic material present.

3. Considerations of an iron core and iron-rich layer

The whole-moon permeability has also been used to investigate the magnetic effects of a hypothetical iron core in the moon. Density and moment of inertia measurements for the moon limit the size of such a core to less than 500 km in radius (Toksöz, 1974). If this hypothetical iron core were entirely paramagnetic and the surrounding core were orthopyroxene of average temperature $1100^{\circ}C$ the global permeability would be 1.0003. This value is small compared to the measured permeability of 1.012 ± 0.006, implying that if such a small paramagnetic iron core exists, its magnetization is masked by magnetic material lying nearer to the surface. Therefore the hysteresis measurements can neither confirm nor rule out the existence of a small iron core in the moon.

An iron-rich layer in the moon has been considered by several investigators (e. g. , Wood et al. , 1970; Urey et al. , 1971; Gast and Giuli, 1972). It is possible that early melting and subseq: ent differention of the outer several hundred kilometers of the moon may have resulted in the formation of a high-density, iron-rich layer beneath a low-density, iron-depleted crust. Constraints have been placed on an iron-rich layer by Gast and Giuli (1972) using geochemical and geophysical data (for example, measurements of lunar moments of inertia). One set of their models consists of high-density layers between depths of 100 km and 300 km. At a depth of 100 km the allowed layer thickness is 12 km; the thickness increases with increasing depth, to 50 km at 300 km depth. Also presented are a set of layers at 500 km depth. By using exactly the same considerations as were used in the iron abundance calculations, calculations have been made of the whole-moon permeabilities which would be expected from lunar models with these iron-rich layers (Parkin et al. , 1974a, b). The calculations indicate that all iron rich layers allowed by geophysical constraints as outlined by Gast and Giuli, if wholly above the iron Curie temperature and therefore paramagnetic, would yield global permeabilities of about 1.00006. As for the case of a small lunar iron core, the magnetization field of such paramagnetic layers would be masked by ferromagnetic materials elsewhere in the moon, and the hysteresis curve measurements can neither confirm nor rule out these layers. This conclusion would particularly apply to the Gast-Giuli layers at 500 km depths, which are almost certainly paramagnetic. If the

Iron-rich layers are below the Curie temperature and therefore ferromagnetic, they would yield measured global permeabilities of about 3.5. This value is well above the upper limit for the actual measured permeability of 1.012 ± 0.006, and therefore the Gast-Giuli layers can be ruled out if they are cool enough to be ferromagnetic. It is important to note that the high-density layers discussed by Gast and Giuli (1972) can be thought of as limiting cases and that there are innumerable less dense and thinner layers which are allowed by geophysical, geochemical and magnetic constraints.

LUNAR REMANENT MAGNETIC FIELDS AND INTERACTIONS WITH THE SOLAR WIND

The permanent magnetic fields of the moon have been investigated using surface magnetometer measurements at four Apollo sites, orbital measurements from Explorer 35 and two Apollo subsatellite magnetometers, and natural remanent magnetization measurements of returned lunar samples. Lunar remanent field measurements by surface magnetization measurements have been considered elsewhere (Hinners, 1971; Nagata et al., 1972; Strangway et al., 1973a; Fuller, 1974).

The permanent lunar magnetic fields were first measured in situ by the Apollo 12 lunar surface magnetometer (LSM) which was deployed on the eastern edge of Oceanus Procellarum. The permanent field magnitude was measured to be 38 ± 3 gammas and the source of this field was determined to be local in extend (Dyal et al., 1970b; Barnes et al., 1971). A remanent field this large was generally unexpected even though relatively strong natural remanent magnetism had been discovered in the Apollo 11 samples, and the explanation of the field's origin yet remains a central problem in lunar magnetism. Subsequent to this measurement of an intrinsic lunar magnetic field, surface magnetometers have measured fields at the Apollo 14, 15 and 16 sites. Fields of 103 ± 5 and 43 ± 6 gammas, at two sites located about a kilometer apart, were measured by the Apollo 14 Lunar portable magnetometer (LPM) at Fra Mauro. A steady field of 3.4 ± 2.9 gammas was measured near Hadley Rille by the Apollo 15 LSM. At the Apollo 16 landing site both a portable and stationary magnetometer were deployed; magnetic fields ranging between 112 and 327 gammas were measured at five different locations over a total distance of 7.1 kilometers at the Descartes landing site. The Apollo 16 fields are the largest lunar fields yet

measured. A schematic representation of these measured field vectors is shown
in Figure 13. All the vectors have components pointing downward except the one
at Site 5 near Stone Mountain, which points upward. This suggests, among other
possibilities, that the material underlying Stone Mountain has undergone different
geological processes than that underlying the Cayley Plains and North Ray Crater.
In fact, Strangway et al. (1973b) have proposed the possibility that the light colored,
relatively smooth Cayley formation is magnetized roughly vertically; the difference
in the vertical component at site 5 is explained as an edge effect at the Cayley Plains -
Stone Mountain boundary. A summary of all remanent lunar fields measured by the
magnetometer deployed on the surface is given in Table 1.

Interaction of the solar wind with the remanent magnetic field has been measured
at the Apollo 12 and 16 landing sites. The solar plasma is directly measured at the
Apollo 12 and 15 sites (Clay et al., 1972) and simultaneous magnetic field and plasma
data show a compression of the steady field as a function of the solar wind pressure
at the Apollo 12 and 16 sites (Dyal et al., 1973). The nature of the correlation between
magnetic field and plasma bulk flow pressures is shown in Figure 14, which shows
data (combined from several lunations) at the Apollo 12 and 16 LSM sites. The plasma
bulk flow pressure and the magnetic pressure are related throughout the measurement
range, and the magnitudes of magnetic pressure changes are in proportion to the
unperturbed steady field magnitudes at each site.

Information on the scale sizes of the permanently magnetized regions near Apollo
landing sites is given by gradient measurements of the lunar surface magnetometers, the
spacing of vector measurements over the lunar surface, the known interaction
properties of these remanent fields with the solar wind plasma, and limits imposed
by satellite measurements. The field gradient in a plane parallel to the lunar surface
is less than the instrument resolution of 0.13 gamma/meter at the Apollo 12 and 15 sites.
At Apollo 14 a field difference of 60 gammas was measured at two sites located 1.1 km
apart. Gradient measurements and the absence of changes in the permanent field at
the sites after lunar module ascent have demonstrated that the field sources are not
magnetized artifacts.

The scale size of the Apollo 12 remanent field has been calculated from local
gradient and Explorer 35 measurements to be from 2 km to 200 km (Dyal et al., 1972b).
For the Apollo 16 field, portable magnetometer measurements over the lunar roving

vehicle traverse have shown that the scale size for the field is greater than 5 km; the Apollo 16 subsatellite magnetometer has shown no anomalous field attributable to the Descartes area at orbital altitude, implying a surface field scale size upper limit of 100 km. Therefore, the Apollo 16 remanent field scale size is between 5 and 100 km.

PROPERTIES OF THE EARTH'S MAGNETOPAUSE AND BOW SHOCK

Using simultaneous data from a net work of magnetometers on the lunar surface
and in orbit around the moon, the velocity and thickness of the geomagnetic magnetopause
and bow shock have been measured at the lunar orbit (Daily et al., 1974). Elapsed-time
data for shock and magnetopause motions as measured by magnetometers separated up
to 10^4 km from each other, indicate that these boundaries are nearly always in motion
and can have highly variable velocities. The magnetopause has an average speed of
about 50 km/sec but measurements vary from less than 10 km/sec up to about 150
km/sec. Similarly, the bow shock has an average speed of about 70 km/sec but again
there is a large spread in measured values from less than 10 km/sec to about 200 km/sec.
Based on the calculated boundary speeds and the signature of the boundary in the
magnetometer data, the thickness of the bow shock and magnetopause have been estimated.
The average measured magnetopause thickness is about 2300 km; however,
individual magnetopause boundaries range from 500 km to 5000 km in thickness. The
average bow shock thickness is determined to be about 1400 km, with a spread in
individual values ranging from 220 km to 3000 km.

SUMMARY

1. Lunar electrical conductivity and temperature

The electrical conductivity of the lunar interior has been investigated by analyzing the induction of global lunar fields by time varying extralunar (solar or terrestrial) magnetic fields. An upper limit on the unipolar induction field has been determined (Dyal and Parkin, 1971b) which shows that at least the outer 5 km of the lunar crust is a relatively poor electrical conductor ($< 10^{-9}$ mhos/m) compared to the underlying material. Past conductivity analyses have all used magnetometer data recorded at times when global eddy current fields were asymmetrically confined by the solar wind plasma, using two basic approaches: a time-dependent, transient-response technique and a frequency-dependent, Fourier-harmonic technique. Transient analysis using lunar nightside data yields a conductivity profile rising from about 3×10^{-4} mhos/meter at 170 km depth in the moon to about 10^{-2} mhos/meter at 1000 km depth.

Recent conductivity analysis has considered lunar eddy current response during times when the moon is in the geomagnetic tail in order to avoid the analytical problems posed by asymmetric solar wind confinement of the induced lunar magnetosphere. Preliminary results show that the following conductivity profile, though not unique, is compatible with input and response data: the conductivity increases rapidly with depth from 10^{-9} mhos/meter at the surface to 10^{-4} mhos/meter at 340 km depth, then less rapidly to 2×10^{-2} mhos/meter at 870 km depth. This conductivity profile is converted to a lunar temperature profile using the data of Duba et al. (1972) for olivine, and compared to the thermal profile results from other analyses.

2. Lunar magnetic permeability and iron abundance

Simultaneous measurements by lunar magnetometers on the surface of the moon and in orbit around the moon have been used to construct a whole-moon hysteresis curve, from which the global lunar relative magnetic permeability is determined to be 1.012 ± 0.006. The global induced magnetization dipole moment corresponding to the permeability measurement is 2×10^{22} H (where H is magnetizing field in gauss). For typical geomagnetic tail fields of $H \sim 10^{-4}$ gauss, the corresponding induced dipole moment is 2×10^{18} gauss-cm^3. Both error limits on the magnetic permeability value are greater than 1.0, implying

that the moon as a whole is paramagnetic and/or weakly ferromagnetic. Assuming that the ferromagnetic component is free metallic iron of multidomain, noninteracting grains, the free iron abundance in the moon is calculated to be 2.5 ± 2.0 wt. %. Total iron abundance in the moon is determined by combining free iron and paramagnetic iron components for two assumed lunar compositional models. For an orthopyroxene moon of overall density 3.34 g/cm^3 with free iron dispensed uniformly thoughout the lunar interior, the total iron abundance is 12.8 ± 1.0 wt. %. For a free iron/olivine moon the total iron abundance is 5.5 ± 1.2 wt. %.

3. Lunar remanent magnetic fields

Direct measurements of remanent fields have been made at nine sites on the lunar surface: 38 γ at Apollo 12 in Oceanus Procellarum; 103 γ and 43 γ at two Apollo 14 sites separated by 1.1 km in Fra Mauro; 3 γ at the Apollo 15 Hadley Rille site; and 189 γ, 112 γ, 327 γ, 113 γ, and 235 γ at five Apollo 16 sites in the Descartes region, over a distance of 7.1 km. Simultaneous data from Apollo surface magnetometers and solar wind spectrometers show that the remanent fields at the Apollo 12 and 16 sites are compressed by the solar wind. In response to a solar wind dynamic pressure increase of 1.5×10^{-7} dynes/cm^2, the 38 gamma remanent field at the Apollo 12 LSM site is compressed to 54 gammas, whereas the field at the Apollo 16 LSM site correspondingly increases from 235 gammas to 265 gammas. Scale sizes of fields at the Apollo 12 and 16 sites have been determined from properties of the remanent field–plasma interaction and orbiting magnetometer measurements. The Apollo 12 scale size L is in the range $2 \text{ km} \leq L \leq 200$ km, whereas for Apollo 16, $5 \text{ km} \leq L < 100$ km.

There is no direct evidence that a global permanent field exists on the moon at present. Analysis of Apollo subsatellite magnetometer data (Russell et al., 1973) has yielded an upper limit of 4.4×10^{13} gauss-cm^3 for the global permanent field dipole moment.

Measurements by lunar orbiting satellite magnetometers and the Apollo surface magnetometers, and remanence in the returned samples, have yielded strong evidence that the lunar crustal material is magnetized over much of the lunar globe. The origin of the lunar remanent field remains an enigma. Possibilities are generally grouped under three classifications: a strong external (solar or terrestrial) field, an ancient intrinsic field of global scale, and smaller localized field sources.

4. Velocity and thickness of the earth's magnetopause and bow shock

Velocities and thicknesses of the earth's magnetopause and bow shock have been estimated from simultaneous magnetometer measurements. Average speeds are about 50 km/sec for the magnetopause and about 70 km/sec for the bow shock, with large spreads in individual measured values. Average thicknesses are about 2300 km for the magnetopause and 1400 km for the bow shock, again with large spreads in individual measured values.

REFERENCES

Barnes, A., P. Cassen, J. D. Mihalov, and A. Eviatar, Permanent lunar surface magnetism and its deflection of the solar wind, Science, 171, 716-718, 1971.

Behannon, K. W., Intrinsic magnetic properties of the lunar body, J. Geophys. Res., 73, 7257, 1968.

Clay, D. R., B. E. Goldstein, M. Neugebauer, and C. W. Synder, Solar wind spectrometer experiment, in Apollo 15 Preliminary Science Report, NASA SP-289, pp. 10-1 to 10-7, 1972.

Daily, W. D., P. Dyal, C. W. Parkin, Magnetopause velocity and thickness determined from a network of Apollo magnetometers (ABS.), Trans, Amer. Geophys. Union (EOS), 55, 390, 1974.

Duba, A., and A. E. Ringwood, Electrical conductivity, internal temperatures and thermal evolution of the moon, The Moon, 7, 356, 1973.

Duba, A., H. C. Heard, and R. N. Schock, The lunar temperature profile, Earth Planet. Sci. Letters, 15, 301, 1972.

Dyal, P., and C. W. Parkin, Electrical conductivity and temperature of the lunar interior from magnetic transient response measurements, J. Geophys. Res., 76, 5947-5969, 1971a.

Dyal, P., and C. W. Parkin, The Apollo 12 magnetometer experiment: Internal lunar properties from transient and steady magnetic field measurements, Proc. Second Lunar Sci. Conf., Geochim. Cosmochim. Acta, Suppl. 2, Vol. 3, 2391, MIT Press, 1971b.

Dyal, P. and C. W. Parkin, Global electromagnetic induction in the moon and planets, Phys. Earth Planet, Interiors 7, 251, 1973.

Dyal, P., C. W. Parkin, C. P. Sonett, and D. S. Colburn, Electrical conductivity and temperature of the lunar interior from magnetic transient response measurements, NASA TMX-62012, 1970a.

Dyal, P., C. W. Parkin, and C. P. Sonett, Apollo 12 magnetometer: Measurement of a steady magnetic field on the surface of the moon, Science, 169, 762, 1970b.

Dyal, P., C. W. Parkin, and P. Cassen, Surface magnetometer experiments: Internal lunar properties and lunar surface interactions with the solar plasma, Proc. Third Lunar Sci. Conf., Geochim. Cosmochim. Acta, Suppl. 3, Vol. 3, p. 2287, edited by D. R. Criswell, MIT Press, 1972a.

Dyal, P., C. W. Parkin, C. W. Synder, and D. R. Clay, Measurements of lunar magnetic field interaction with the solar wind, Nature, 236, 381-385, 1972b.

Dyal, P., C. W. Parkin, and W. D. Daily, Surface magnetometer experiments: Internal lunar properties, Proc. Fourth Lunar Science Conf., Geochim. Cosmochim. Acta, Suppl. 4, edited by W. A. Gose, Vol. 3, pp. 2229-2945, Pergamon, 1973.

Dyal, P., C. W. Parkin, and W. D. Daily, Magnetism and the interior of the moon, submitted to Rev. Geophys. Space Phys., 1974.

Ellwood, W. B., A new ballistic galvanometer operating in high vacuum, Rev. Sci. Inst., 5, 300-305, 1934.

England, A. W., G. Simmons, and D. Strangway, Electrical conductivity of the moon, J. Geophys, Res., 73, 3219, 1968.

Fuller, M., Lunar magnetism, Rev. Geophys. Space Phys., in press, 1974.

Gast, P. W., and R. T. Giuli, Density of the lunar interior, Earth Planet. Sci. Letters, 16, 299, 1972.

Green, D. H., A. E. Ringwood, N. G. Ware, W. O. Hibberson, A. Major, and E. Kiss, Experimental petrology and petrogenesis of Apollo 12 basalts, Proc. Second Lunar Sci. Conf., Geochim, Cosmochim. Acta, Suppl. 2, Vol. 1 edited by A. A. Levinson, MIT Press, 601-615, 1971.

Hinners, N. W., The new moon: A view, Rev. Geophys. Space Phys., 9, 447, 1971.

Kuckes, A. F., Lunar electrical conductivity profile, Nature, 232, 249, 1971.

Kuckes, A. F., P. Dyal, W. D. Daily, and C. W. Parkin, Temperature profile of the moon, submitted to Nature, 1974.

Nagata, T., R. M. Fisher, F. C. Schwerer, M. D. Fuller, and J. R. Dunn, Magnetic properties and remanent magnetization of Apollo 12 lunar materials and Apollo 11 lunar microbreccia, Proc. Second Lunar Sci. Conf., Geochim. Cosmochim. Acta, Suppl. 2, Vol. 3, 2461, edited by A. A. Levinson, MIT Press, 1971.

Nagata, T., R. M. Fisher, F. C. Schwerer, M. D. Fuller, and J. R. Dunn, Rock magnetism of Apollo 14 and 15 materials. Proc. Third Lunar Sci. Conf. Geochim. Cosmochim. Acta, Suppl. 3, Vol. 3, p. 2423, edited by D. R. Criswell, MIT Press, 1972.

23

Olhoeft, G. R., A. L. Frisillo, D. W. Strangway, and H. Sharpe, Electrical properties of lunar solid samples, in Lunar Science IV, edited by J. Chamberlain and C. Watkins, The Lunar Science Institute, Houston, pp. 575-577, 1973.

Parkin, C. W., P. Dyal and W. D. Daily, Iron abundance in the moon from magnetometer measurements, Proc. Fourth Lunar Sci. Conf., Geochim. Cosmochim. Acta, Suppl. 4, Vol. 3, p. 2947, edited by W. A. Gose, Pergamon Press, 1973.

Parkin, C. W., W. D. Daily and P. Dyal, Iron abundance in the moon, submitted to Astrophys. J., 1974a.

Parkin, C. W., W. D. Daily, and P. Dyal, Lunar iron abundance from magnetometer measurements, in Lunar Science V, Part II, p. 589, The Lunar Science Institute, Houston, 1974b.

Pearce, G. W., D. W. Strangway, and E. E. Larson, Magnetism of two Apollo 12 igneous rocks, Proc. Second Lunar Sci. Conf., Geochim. Cosmochim. Acta, Suppl. 2, Vol. 3, p. 2451, edited by A.A. Levinson, MIT Press, 1971.

Reisz, A. C., D. L. Paul, and T. R. Madden, The effects of boundary condition asymmetries on the interplanetary magnetic field-moon interaction, The Moon, 4, 134-140, 1972.

Reynolds, R. T., and A. L. Summers, Calculations on the composition of the terrestrial planets, J. Geophys. Res., 74, 2494, 1969.

Rikitake, T., Electromagnetism and the Earth's Interior, Elsevier, Amsterdam, 1966.

Ringwood, A. E., and E. Essene, Petrogenesis of lunar basalts and the internal constitution and origin of the moon, Science. 167, 607-610, 1970.

Russell, C. T., P. J. Coleman, Jr., B. R. Lichtenstein, G. Schubert, and L. R. Sharp, Subsatellite measurements of the lunar magnetic field, Proc. Fourth Lunar Sci. Conf., Geochim. Cosmochim. Acta, Suppl. 4, edited by W. A. Gose, Vol. 3, pp. 2833-2845, 1973.

Schubert, G., B. F. Smith, C. P. Sonett, D. S. Colburn., and K. Schwartz, The nightside electromagnetic response of the moon, J. Geophys. Res., 78, 3688-3696, 1973a.

Schubert, G., C. P. Sonett, K. Schwartz, and H. J. Lee, Induced magnetosphere of the moon 1. Theory, J. Geophys. Res., 78, 2094-2110, 1973b.

Schwartz, K., and G. Schubert, Lunar electromagnetic scattering I. Propagation parallel to the diamagnetic cavity axis, J. Geophys. Res., 78, 6496-6506, 1973.

Schwerer, F. C., G. P. Huffman, R. M. Fisher, and T. Nagata, D. C. electrical conductivity of lunar surface rocks, The Moon, 4, 187, 1972.

Sill, W. R., Lunar conductivity models from the Apollo 12 magnetometer experiment, The Moon, 4, 3-17, 1972.

Smythe, W. R., Static and Dynamic Electricity, McGraw-Hill Book Co., New York, 1950.

Sonett, C. P., D. S. Colburn, P. Dyal, C. W. Parkin, B. F. Smith, G. Schubert, and K. Schwartz, Lunar electrical conductivity profile, Nature, 230, 359, 1971.

Sonett, C. P., B. F. Smith, D. S. Colburn, G. Schubert, and K. Schwartz, The induced magnetic field of the moon: conductivity profiles and inferred temperature, Proc. Third Lunar Sci. Conf., Geochim. Cosmochim. Acta, Suppl. 3, Vol. 3, edited by D. R. Criswell, The MIT Press, p. 2309, 1972.

Strangway, D. W., W. A. Gose, G. W. Pearce, and J. G. Carnes, Magnetism and the history of the moon, Proc. of the 18th Annual Conf. on Magnetism and Magnetic Materials, J. Applied Phys., in press, 1973a.

Strangway, D. W., W. A. Gose, G. W. Pearce, and R. K. McConnell, Lunar magnetic anomalies and the Cayley formation, Nature, 246, 112, 1973b.

Toksöz, M. N., Geophysical data and the interior of the moon, Ann. Rev. Earth and Planet. Sci, In Press, 1974.

Urey, H. C., The Moon, ed. Z. Kopal and Z. K. Mikhailov, p. 133, Academic Press, 1962.

Urey, H. C. and G. J. F. MacDonald, Origin and history of the moon, in Physics and Astronomy of the Moon, edited by Z. Kopal, p. 213, Academic Press, 1971.

Wait, J. R., A conducting sphere in a time varying magnetic field, Geophysics, 16, 666, 1951.

Wänke, H., H. Baddenhausen, G. Driebus, M. Quijano-Rico, M. Palme, B. Spettel, and F. Teschke, Multielement analysis of Apollo 16 samples and about the composition of the whole moon, in Lunar Science IV, editors J. W. Chamberlain and C. Watkins, pp. 761-763, Lunar Science Institute, Houston, 1973.

Weeks, R. A., Magnetic phases in lunar material and their electron magnetic resonance spectra: Apollo 14., Proc. Third Lunar Sci. Conf., Geochim. Cosmochim. Acta, Suppl. 3, Vol. 3, 2503, MIT Press, 1972.

Wood, J. A., J. S. Dickey, U. B. Marvin, and B. J. Powell, Proc. Apollo 11 Lunar Sci. Conf. Geochim. Cosmochim. Acta, Suppl. 1, Vol. 1, p. 965, edited by A. A. Levinson, Pergamon Press, 1970.

Zussman, J., The minerology, petrology and geochemistry of lunar samples - a review, The Moon, 5, 422, 1972.

Table 1. Summary of Lunar Surface Remanent Magnetic Field Measurements.

Site	Coordinates, deg.	Field Magnitude, Gammas	Magnetic-field components, gammas		
			Up	East	North
Apollo 16:					
ALSEP Site	8.9°S, 15.5°E	235 ± 4	-186 ± 4	-48 ± 3	+135 ± 3
Site 2		189 ± 5	-189 ± 5	+3 ± 6	+10 ± 3
Site 5		112 ± 5	+104 ± 5	-5 ± 4	-40 ± 3
Site 13		327 ± 7	-159 ± 6	-190 ± 8	-214 ± 6
LRV Final Site		113 ± 4	-66 ± 4	-76 ± 4	+52 ± 2
Apollo 15:					
ALSEP Site	26.1°N, 3.7°E	3.4 ± 2.9	+3.3 ± 1.5	+0.9 ± 2.0	-0.2 ± 1.5
Apollo 14:	3.7°S, 17.5°W				
Site A		103 ± 5	-93 ± 4	+38 ± 5	-24 ± 5
Site C'		43 ± 6	-15 ± 4	-36 ± 5	-19 ± 8
Apollo 12:					
ALSEP Site	3.2°S, 23.4°W	38 ± 2	-25.8 ± 1.0	+11.9 ± 0.9	-25.8 ± 0.4

FIGURE CAPTIONS

Figure 1.   Apollo magnetometer locations and measurements on the lunar surface.
Maximum remanent magnetic fields measured at each landing site are
shown.   The insert shows an orbit of the Explorer 35 spacecraft, projected
onto the solar ecliptic plane.

Figure 2.   Apollo 16 magnetometers deployed on the moon at the Descartes landing site.
(a) Lunar surface magnetometer (LSM).   Sensors are at the top ends of the
booms, approximately 75 cm above the lunar surface.   (b) Lunar portable
magnetometer (LPM), deployed during a magnetic field measurement by
astronaut Young.   Sensors are located on top of tripod at far right in photograph.

Figure 3.   Magnetic environment of the moon during a lunar orbit, with emphasis on
the geomagnetic tail region.   The plane of the lunar orbit very nearly
coincides with the ecliptic plane of the earth 's orbit.   The earth's permanent
dipole field is swept back into a cylindrical region known as the geomagnetic
tail; at the lunar distance the field magnitude is ~ 10 gammas $(10^{-4}$ gauss).
Substructure of the tail includes two lobes which are separated by the neutral
sheet current boundary; the upper or northward lobe has its magnetic field
pointing roughly toward the earth, whereas the southward lobe field points
away from the earth.   The moon is immersed in the tail about four days of each
orbit; the moon can pass through either or both lobes.

Figure 4.   Global eddy current induction with the Moon in the geomagnetic tail.   The
induced poloidal field is considered to be in a vacuum in the deep-lobe regions
of the tail.

Figure 5.   Transient response data, measured when moon was in the solar wind. (a)
Nightside transient response data,   showing decay characteristics of the
radial component of the total surface field B_{Ax} after arrival of a step transient
which reduces the external magnetic field radial component by an amount ΔB_{Ex},
here normalized to one.   The shape of the curve illustrates time characteristics
of the decay of the induced poloidal eddy-current field (from Dyal and Parkin,
1973).   (b) Daytime transient response data, showing decay characteristics of
tangential components $(B_{Ay,z})$ of the total surface field after arrival of a step

transient which increases the external magnetic field tangential component

by an amount $\Delta B_{Ey, z}$, here normalized to one. Shape of the curve again

illustrates decay characteristics of the induced poloidal field. The overshoot

maximum is amplified to ~ 5 by solar wind dayside compression; the

theoretical overshoot maximum is 1.5 for an unconfined poloidal field. (From

Dyal et al., 1973).

Figure 6. Transient event in the geomagnetic tail, measured simultaneously by the

Apollo 12 LSM and the Explorer 35 Ames magnetometer. Data are expressed

in the surface coordinate system which has its origin at the Apollo 12

magnetometer site; x is directed radially outward from the surface, while y

and z are tangent to the surface, directed eastward and northward, respectively.

Due to poloidal field induction in the moon, the Apollo 12 radial (x) component

is "damped" relative to the Explorer 35 radial component, whereas the Apollo 12

tangential (y and z) field components are "amplified" relative to Explorer 35

data. Apollo 12 and Explorer 35 component data scales differ due to the

existence of a 38 ± 3 gamma remanent field at the Apollo 12 surface site.

Figure 7. Electrical conductivity analysis for a transient event in the geomagnetic tail.

Shown are data from the radial component of the event of Figure 6. Response

to the Explorer 35 external field radial component is computed numerically for

the conductivity profile shown in the insert and compared to the measured

Apollo 12 response field. In the preliminary results of geomagnetic tail

conductivity analysis, this selected conductivity profile, though not unique,

yields a satisfactory fit of input and response data for this and twenty other

tail events processed to date.

Figure 8. Electrical conductivity profiles for the lunar interior calculated from

measurements in different regions of the lunar orbit around the earth. The

shaded region (3) is from nightside transient analysis in the solar wind (Dyal

and Parkin, 1973), curve 1 is from dayside transient analysis in the solar

wind, and curve 2 is from transient analysis in the geomagnetic tail (Dyal

et al., 1974).

Figure 9. Temperature profiles of the lunar interior calculated from the conductivity

profile in Figure 8. These calculations use the laboratory data for olivine

from Duba et al. (1972).

Figure 10. Magnetization induction in the moon. When the moon is immersed in a uniform external field $\underline{H}$ (in this case the steady geomagnetic tail field), a dipolar magnetization field $\underline{M}$ is induced in permeable material in the lunar interior, with the dipole axis of $\underline{M}$ aligned along the direction of $\underline{H}$. The total magnetic field near the moon is $\underline{B} = \underline{H} + 4\pi\underline{M}$. The magnetic permeabilities of the two layers are μ_1 and μ_2, and for regions outside the moon, $\mu = \mu_o = 1$ (free space). $\underline{H}$ is measured by the lunar orbiting Explorer 35, whereas $\underline{B}$ is measured by an Apollo lunar surface magnetometer (LSM). Measurements of $\underline{B}$ and $\underline{H}$ allow construction of a B-H hysteresis curve for the sphere, from which permeability and iron abundance can be calculated.

Figure 11. Hysteresis curve for the moon. Data points are 2703 simultaneous 2-minute averages of radial components of the external geomagnetic field data $\underline{H}$ (measured by the lunar orbiting Explorer 35 Ames magnetometer) and total magnetic induction $\underline{B} = \mu\underline{H}$ ($\underline{B}$ is measured by the Apollo 12 lunar surface magnetometer). Data points are selected from four lunations of measurements made when the moon was immersed in the uniform geomagnetic tail field. In this low-external-field regime (~ 10 gammas or 10^{-4} Oe), the hysteresis curve is linear and is fitted by a least-squares line of slope 1.008 ± 0.004. This slope corresponds to a whole-moon magnetic permeability of 1.012 ± 0.006 (from Parkin et al., 1974a, b).

Figure 12. Iron abundance calculated for the moon from the measured global permeability. The percentage of free iron is calculated for a Curie isotherm located at a depth of 260 km in the moon, and the total iron abundance is calculated for two lunar models, (1) a moon composed of free iron and orthopyroxene and (2) a moon composed of free iron and olivine (from Parkin et al., 1974a, b).

Figure 13. Lunar remanent magnetic fields measured at the surface Apollo 16 Descartes sites. (a) Photograph showing the Apollo 16 landing site, the location of the surface magnetometer (LSM), and the traverse positions where the portable magnetometer was deployed. (b) Magnitude and orientation of the measured vector remanent magnetic fields.

Figure 14. Magnetic energy density versus plasma energy density at two Apollo sites which have different remanent magnetic fields. The magnetic energy density is computed from the difference between the compressed and uncompressed remanent field at the Apollo sites. Plasma energy density data are calculated from Apollo solar wind spectrometer (SWS) measurements. N is the proton number density, m is the proton mass, and v is the plasma bulk speed. Apollo 12 magnetometer data are plotted versus Apollo 12 solar wind spectrometer data, while Apollo 16 magnetometer data are plotted versus Apollo 15 SWS data. SWS data are courtesy of C. W. Synder and D. R. Clay of the Jet Propulsion Laboratory. Uncompressed remanent field magnitudes are 38 v at Apollo 12 and 235 v at Apollo 16 LSM sites.

APOLLO 15
3 γ

APOLLO 12
38 γ

APOLLO 14
103 γ (max)

APOLLO 16
327 γ (max)

APOLLO LSM
11.5 hr PERIOD
EXPLORER 35

Fig. 1

Fig. 2

GEOMAGNETIC TAIL

SOLAR WIND

NEUTRAL SHEET

MOON

EARTH

LUNAR ORBIT

BOW SHOCK

Fig. 3

EXTERNAL FIELD CHANGE

EXPLORER 35

LSM

INDUCED FIELD LINES

EDDY CURRENTS
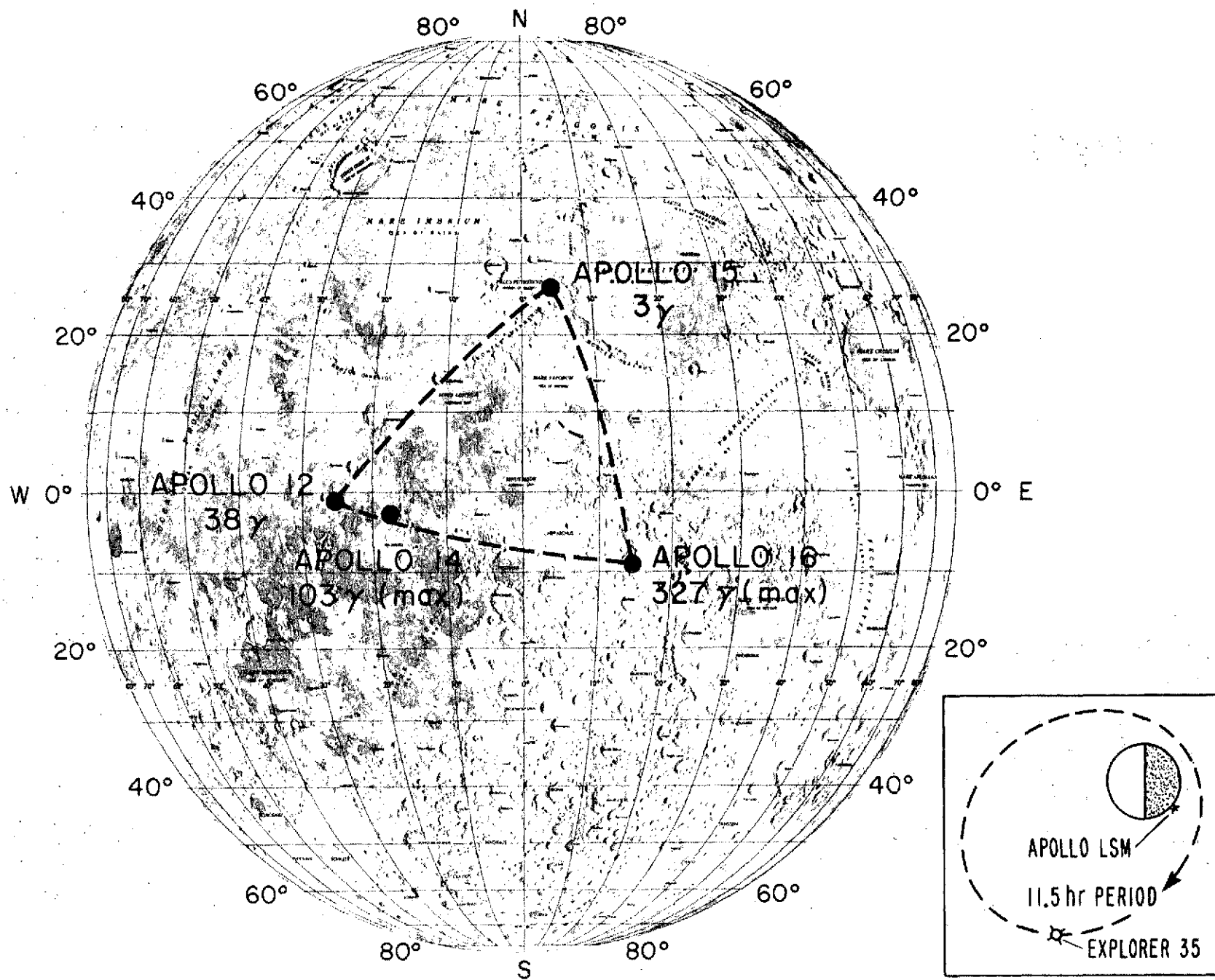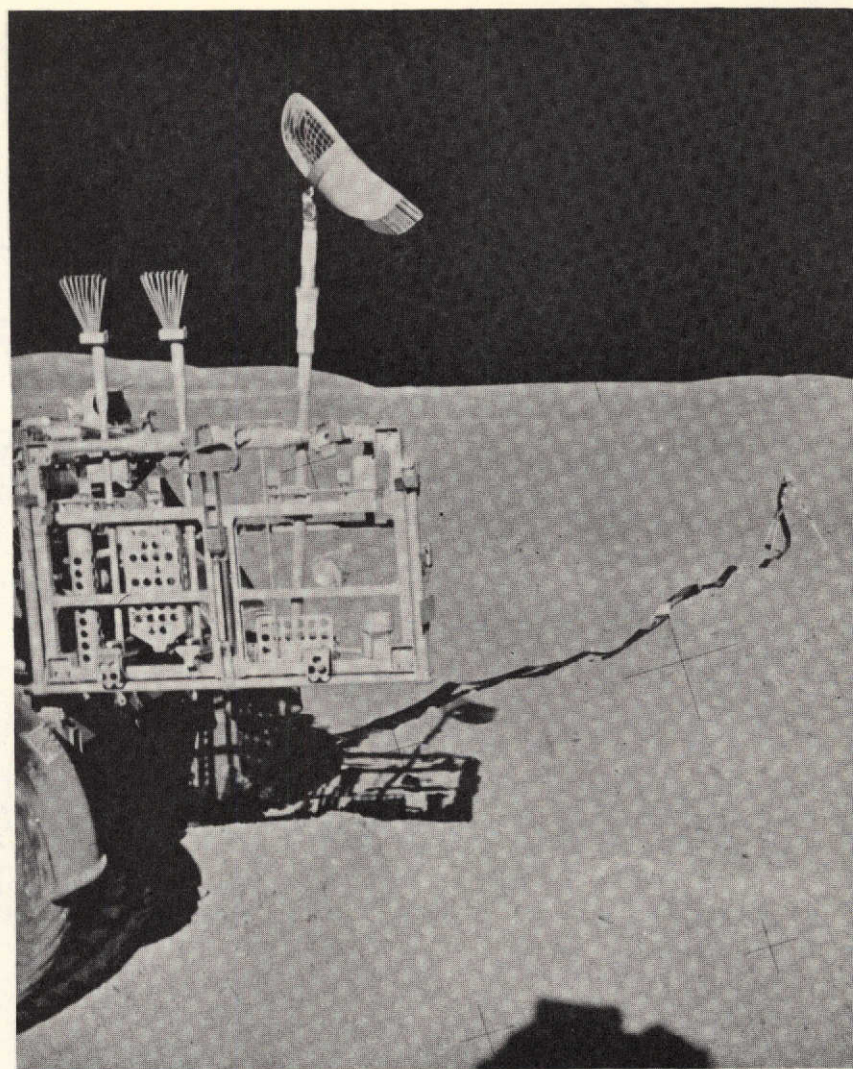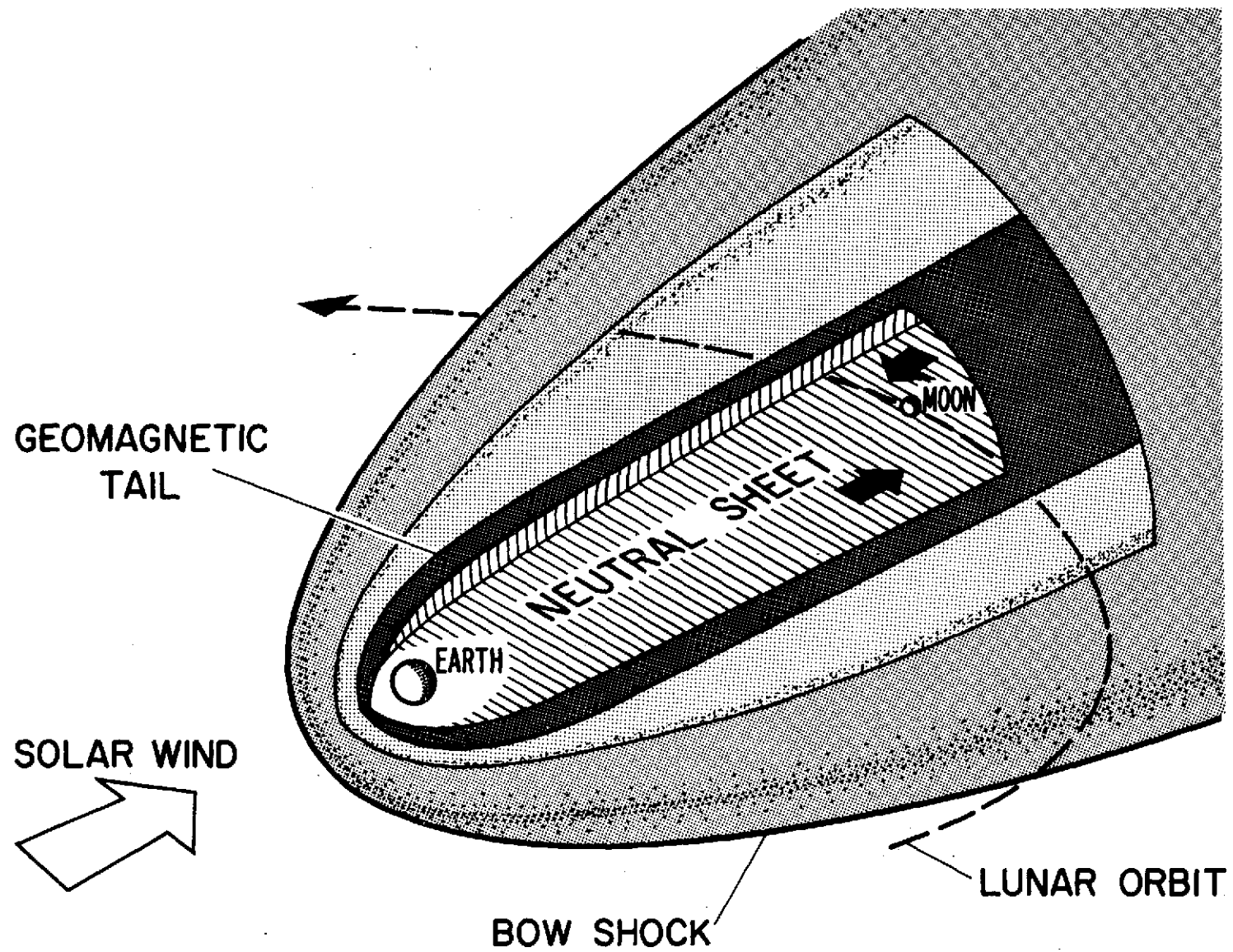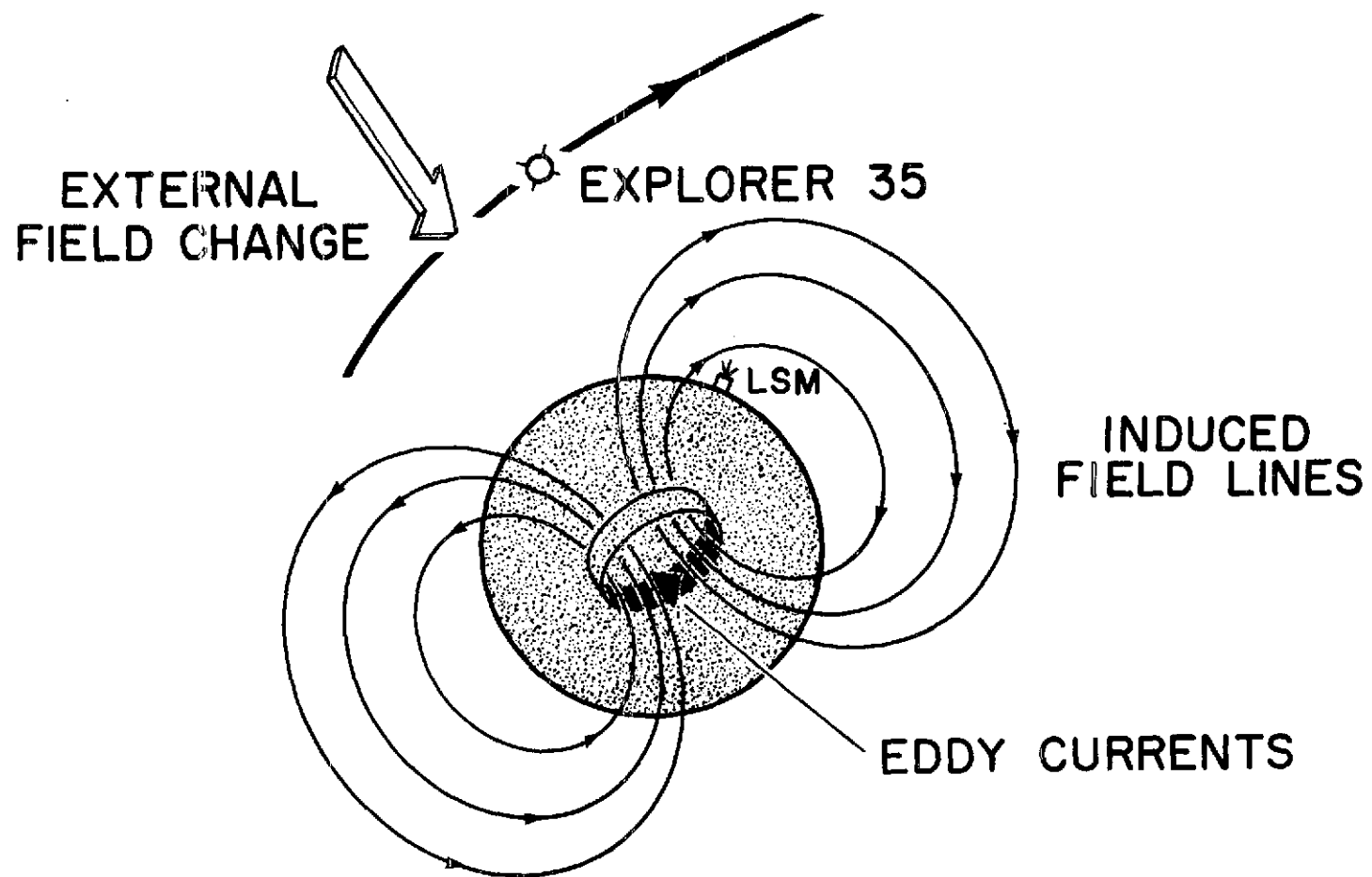
Fig. 4
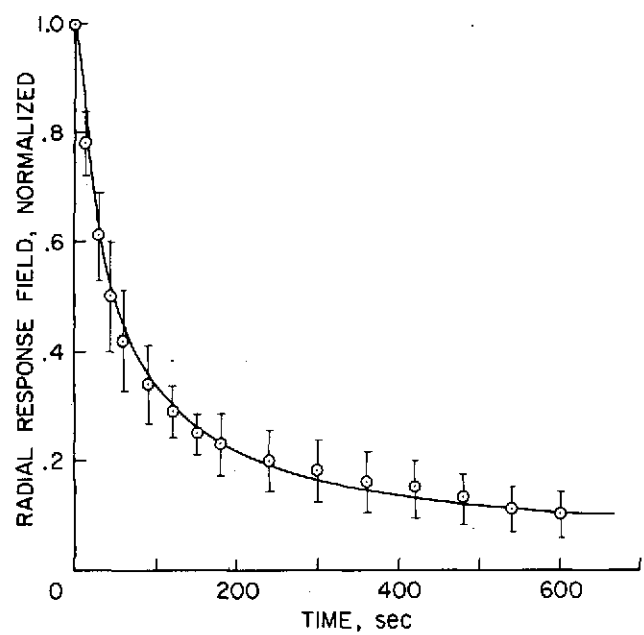
NIGHTSIDE DATA   DAYSIDE DATA
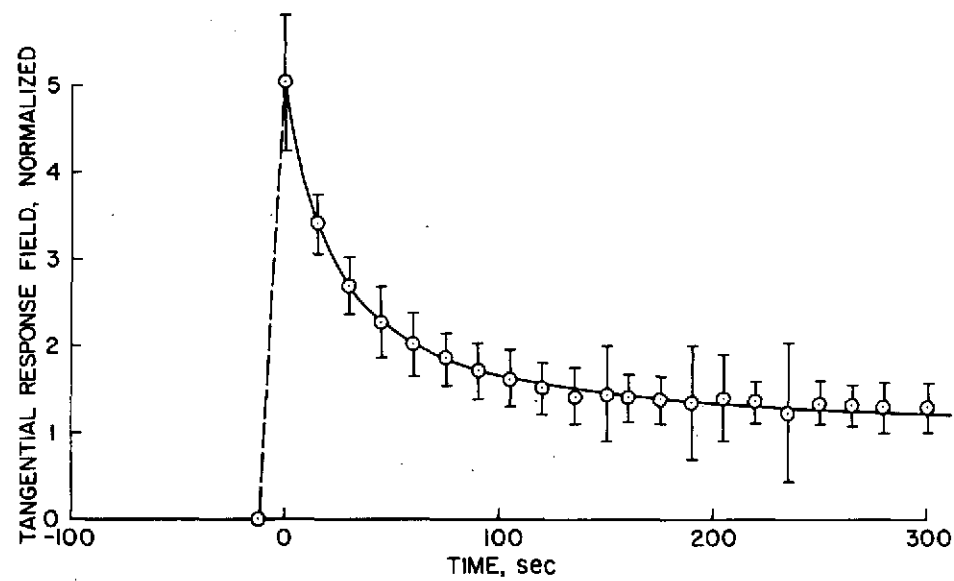
Fig. 5

GEOMAGNETIC TAIL TRANSIENT RESPONSE
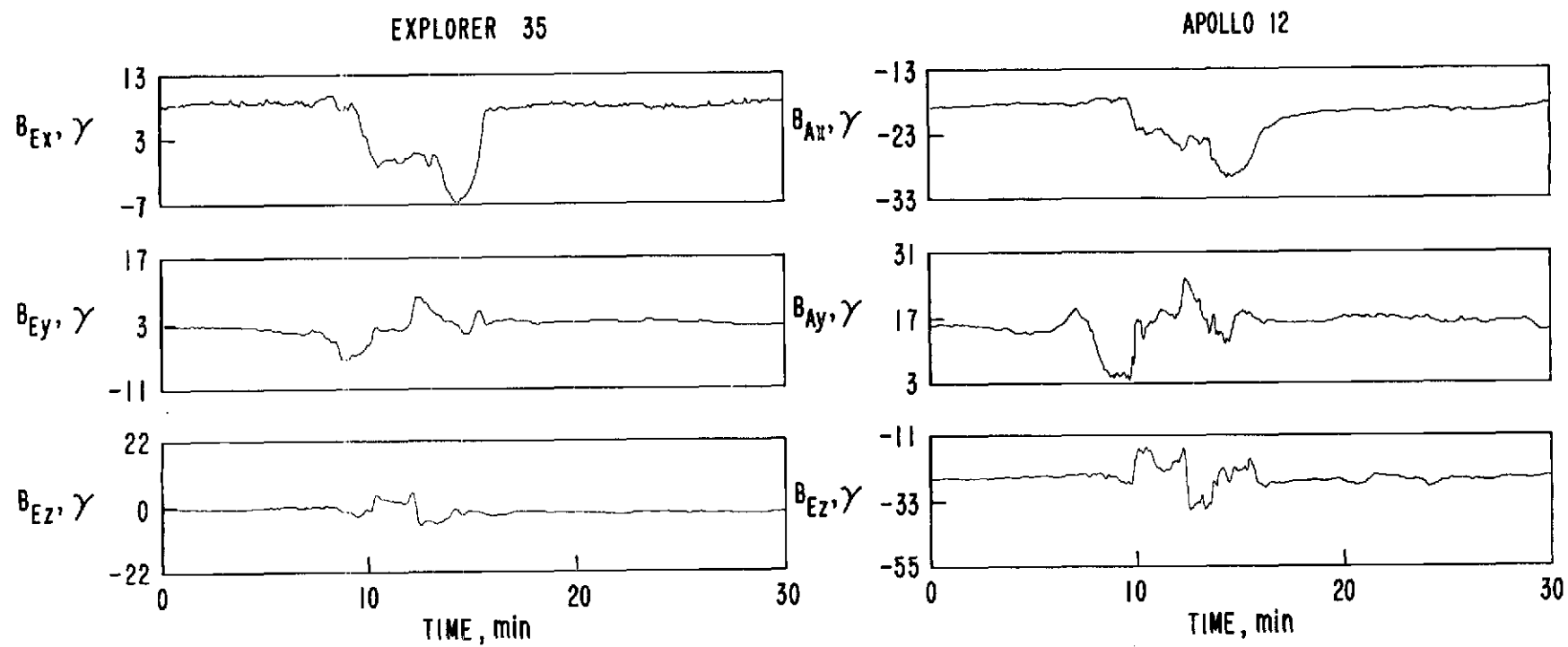
Fig. 6
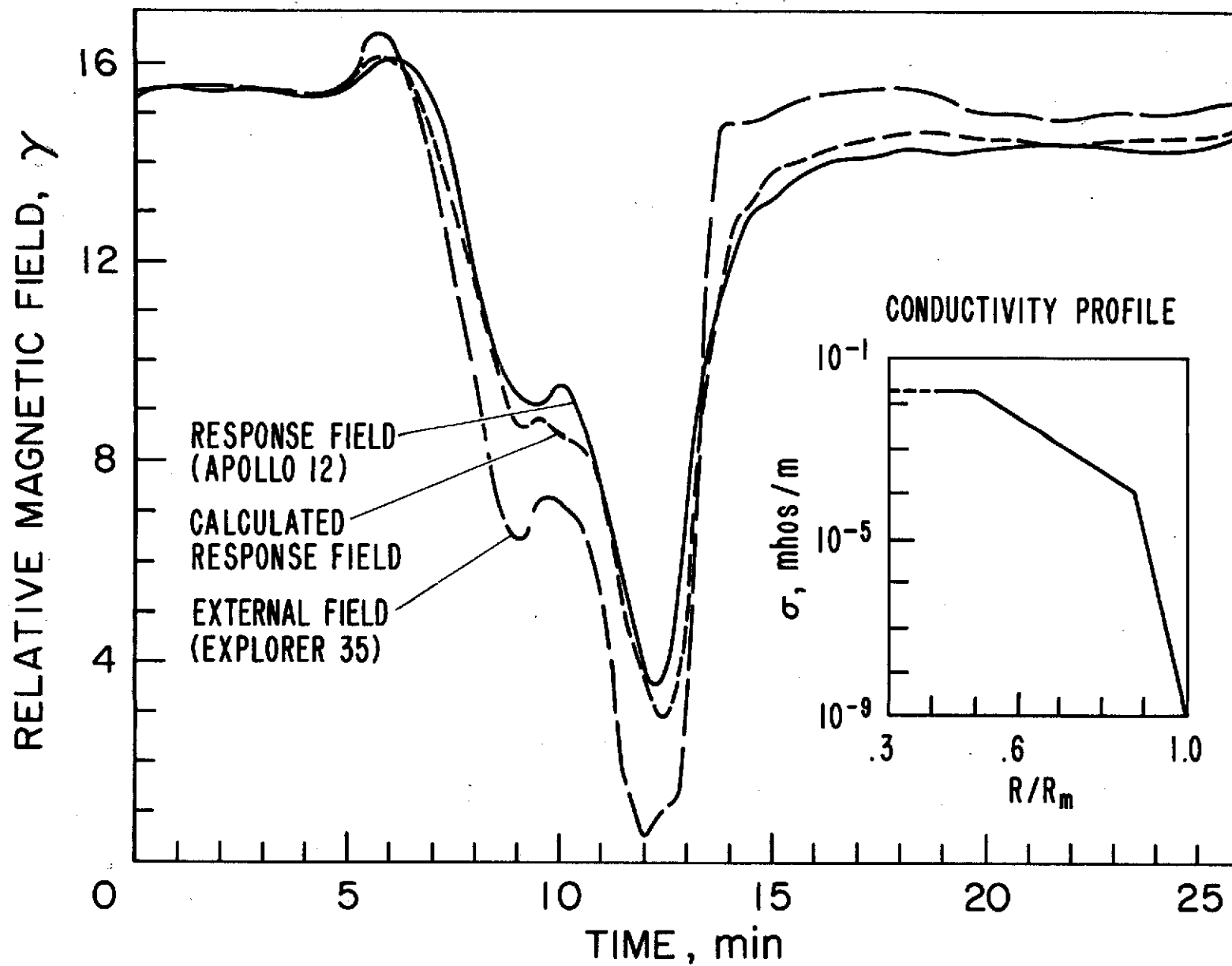
Fig. 7

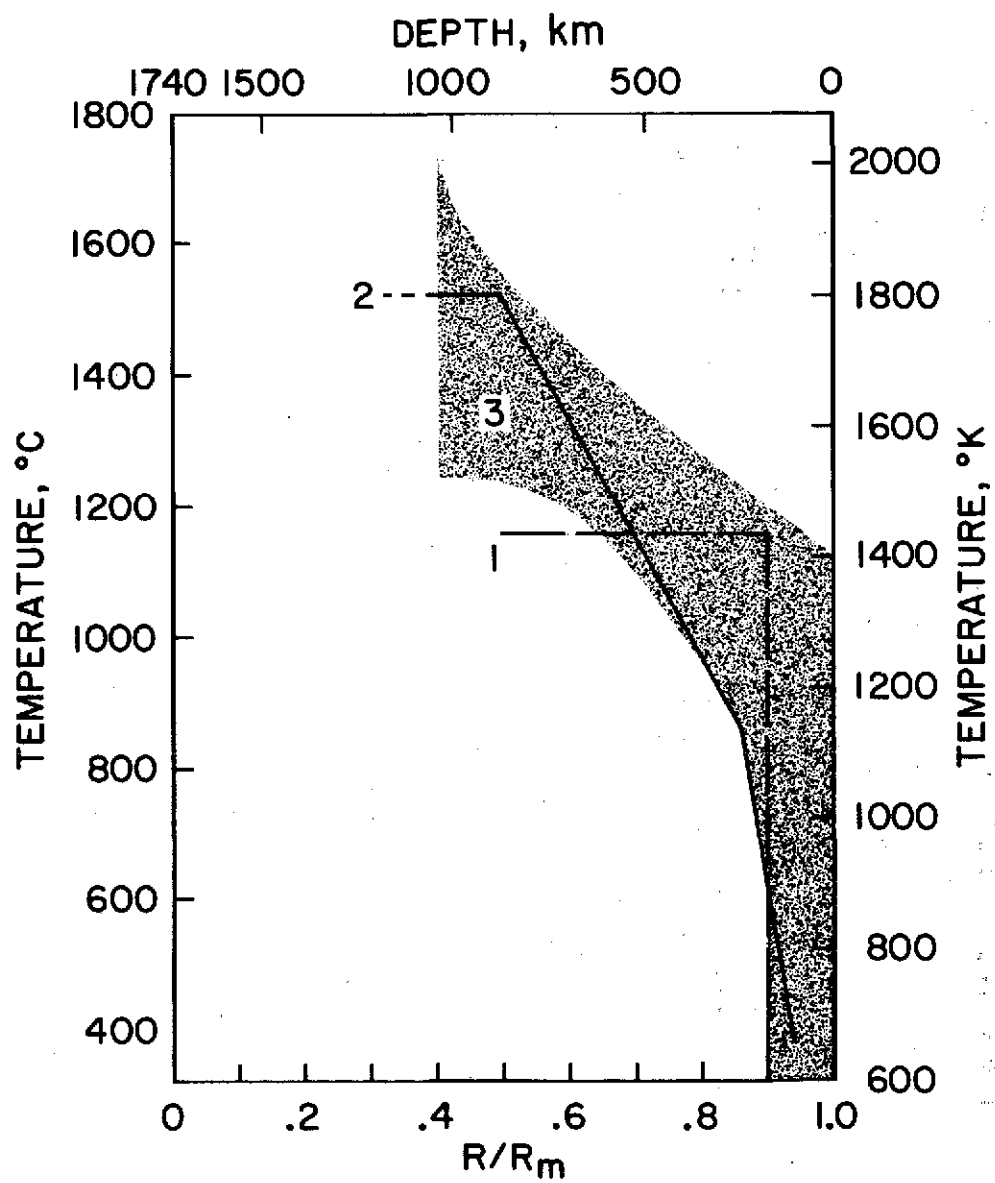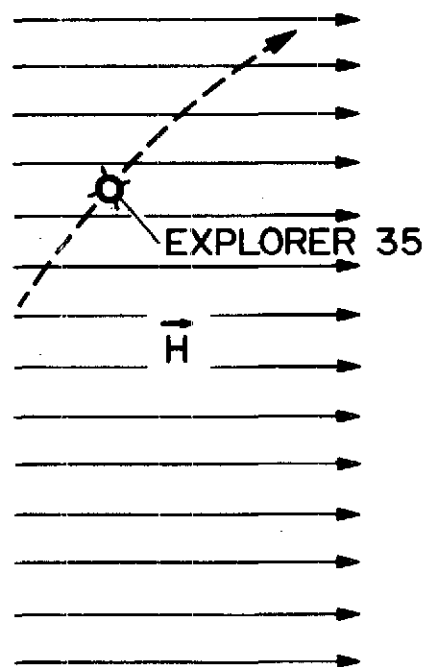# LUNAR CONDUCTIVITY PROFILES
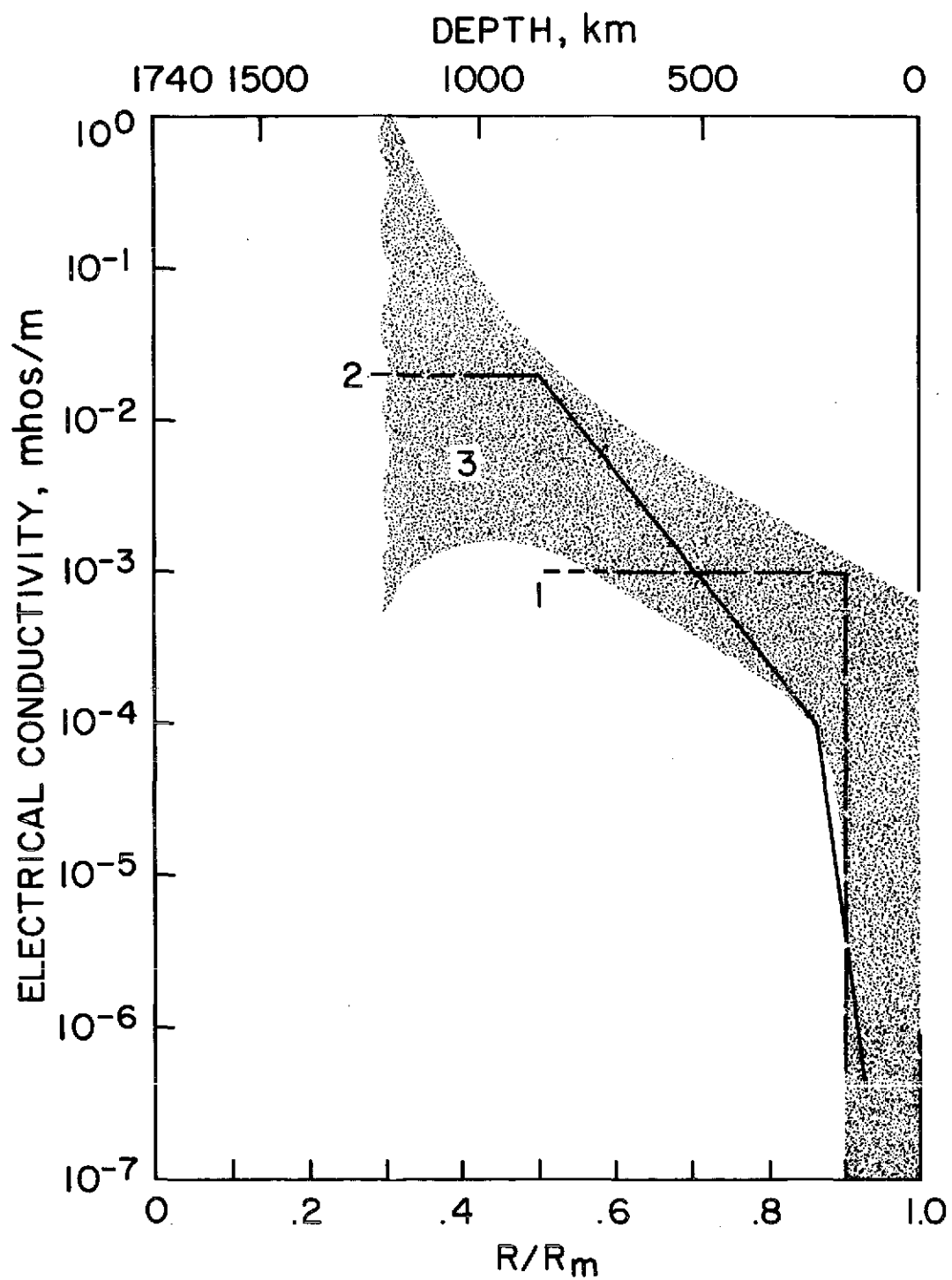
Fig. 8

LUNAR TEMPERATURE PROFILES

Fig. 9

EARTH'S FIELD, $\vec{H}$

FIELD AT MOON, $\vec{B}$

EXPLORER 35

$\vec{H}$

$\vec{B}$

APOLLO

LSM

R_c

R_m

$\mu_0 = 1$

μ_1

μ_2
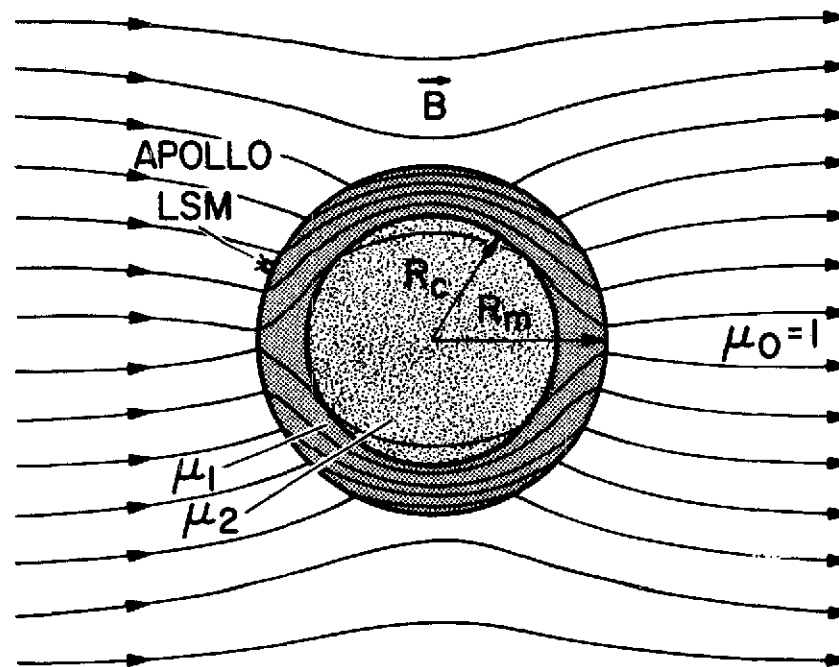
Fig. 10
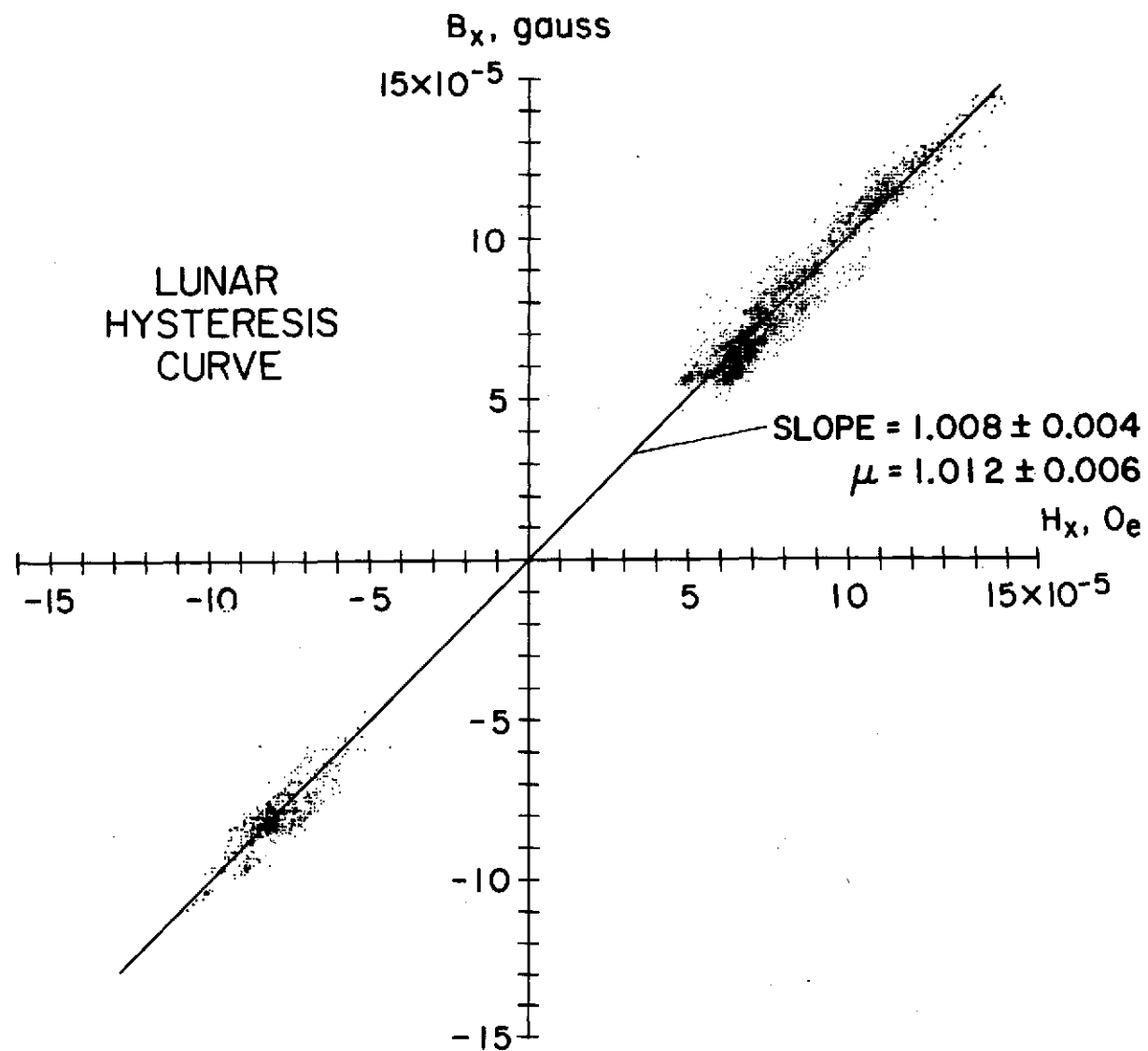
Fig. 11

LUNAR IRON ABUNDANCE

GLOBAL PERMEABILITY: 1.012 ± 0.006

CURIE ISOTHERM
DEPTH: 260 km

FREE IRON: 2.5 ± 2.0 wt.%

TOTAL IRON

    ORTHOPYROXENE/FREE IRON: 12.8 ± 1.0 wt.%

    OLIVINE/FREE IRON: 5.5 ± 1.2 wt.%

Fig. 12

APOLLO 16

Fig. 13

Fig. 14